Journal of
Applied
Crystallography
ISSN 0021-8898

Received 30 September 2004
Accepted 10 November 2004

X-ray scattering from unilamellar lipid vesicles

Michael R. Brzustowicz[b] and Axel T. Brunger[a,b]*

[b]Howard Hughes Medical Institute, USA, and [a]Departments of Molecular and Cellular Physiology, Neurology and Neurological Sciences, and Stanford Synchrotron Radiation Laboratory, J. H. Clark Center Room E300-C, 318 Campus Drive, Stanford, CA 94305-5432, USA. Correspondence e-mail: brunger@slac.stanford.edu

An improved small-angle X-ray scattering (SAXS) method for determining asymmetric lipid bilayer structure in unilamellar vesicles is presented. From scattering theory, analytic expressions are derived for the bilayer form factor over flat and spherical geometries, assuming the lipid bilayer electron density to be composed of a series of Gaussian shells. This is in contrast to both classic diffraction and Guinier hard-shell SAXS methods which, respectively, are capable only of ascertaining symmetric bilayer structure and limited-resolution asymmetric structure. Using model fitting and direct calculation of the form factor, using only one equation, an asymmetric electron density profile of the lipid vesicle is obtained with high accuracy, as well as the average radius. The analysis suggests that the inner leaflet of a unilamellar lipid vesicle is 'rougher' than the outer one.

1. Introduction

Methods for elucidating the structure of lipid bilayers are well established and have provided the basis for our understanding and continued exploration of the detailed molecular shape of biological membranes (Katsaras & Gutberlet, 2001). It is generally thought, under appropriate physiological conditions, that the lipid bilayer exists with its opposing polar head-group regions spaced ∼40 to 50 Å apart (Gennis, 1989) with the volume between filled with hydrocarbon chains. High-resolution studies have revealed many additional features within the bilayer, such as the location of C═C double bonds, carbonyl and phosphoryl moieties and, additionally, guest molecules such as cholesterol and peptides (*e.g.* see White & Hristova, 2001). The bulk of these atomic resolution structural studies have relied on X-ray and neutron diffraction from lipids in the smectic C liquid-crystalline phase commonly called 'aligned bilayers' or 'multilamellar vesicles'. In a typical X-ray diffraction experiment, intense spots and/or rings observed in reciprocal space are used to reconstruct the bilayer electron density map *via* either direct Fourier synthesis or from the Fourier transform of the bilayer form factor. However, due to the well known phase problem in X-ray diffraction, only the magnitude of the form factor is known and the phases must either be obtained from calculation or determined experimentally.

Membranes *in vivo* are far from symmetric: lipids and proteins are distributed asymmetrically across the bilayer since the inner and outer leaflets of the biological membrane each play unique structural and biochemical roles essential for proper cellular functioning (Gennis, 1989). Ideally, one should be able to study this 'sidedness' of the lipid bilayer. In an X-ray or neutron scattering experiment, this is technically feasible using unilamellar lipid vesicles, where Bragg peaks would not appear and only the 'diffuse scattering' from uncorrelated vesicles would exist (Hirai *et al.*, 2003; Pabst *et al.*, 2003; Lesieur *et al.*, 2000; Bouwstra *et al.*, 1993; Kiselev *et al.*, 2001; Nieh *et al.*, 2004). Several of these reports identify membrane asymmetry using a 'hard-shell model' where the vesicle is composed of a series of shells, each with constant electron density (Bouwstra *et al.*, 1993; Hirai *et al.*, 2003). We significantly extend previous models by (*a*) providing an exact analytic expression for the scattering intensity $I(q)$ for unilamellar vesicles, and (*b*) establishing an experimental protocol resulting in a high-quality data set previously not achieved.

We chose *sn*-1-stearoyl-*sn*-2-oleoyl-phosphatidylserine (SOPS) over similar phosphatidylcholine (PC) and phosphatidylethanolamine (PE) systems because of SOPS's larger difference in scattering length density compared with buffer. It is known that very small changes in scattering length density contrast ($\sim 1 \times 10^{-6}$ Å^{-2}) between sample and buffer results in an order of magnitude difference in X-ray scattering amplitude from vesicles (Kiselev *et al.*, 2001). The use of SOPS then resulted in a higher quality data set than previously achieved. From our analysis we find that both flat and spherical models of the bilayer are capable of revealing asymmetric structure, but the spherical model is necessary to obtain information on vesicle size and structure simultaneously. A plausible interpretation of the model fitting suggests that unilamellar lipid vesicles are 'rougher' on the their inner leaflet.

2. Materials and methods

2.1. Sample preparation

SOPS in chloroform was purchased from Avanti Polar Lipids (Alabaster, AL) and used without further purification. After gently removing the chloroform under a stream of argon, the lipids were dissolved in 50 µL cyclohexane and frozen in liquid nitrogen (LN_2). The sample was exposed to vacuum (<10 mTorr) until all the solvent was lyophilized. Initially, the outside of the sample chamber was kept cool with dry ice to ensure that the lipid/solvent mixture remained solid. The resultant fluffy white powder (∼15 mg) was hydrated with 50 m*M* Tris buffer, pH 7.6, to a final concentration of 30 mg ml^{-1}. After gentle vortexing, unilamellar vesicles were formed by passing the mixture through a LiposoFast extruder (Avestin Inc., Canada) ∼21 times using two stacked filters with a pore diameter of 1000 Å. This results in a polydisperse population of mostly spherical, unilamellar vesicles with mean radius ∼400 Å and standard deviation ∼50 Å (MacDonald *et al.*, 1991). 15 µL of the unilamellar vesicle solution was then injected into a solution scattering cell constructed from polycarbonate with thin mica windows, described in detail at http://ssrl.slac.stanford.edu/~saxs.

2.2. X-ray scattering

Small-angle X-ray scattering (SAXS) experiments were performed with synchrotron X-ray radiation at BL 4-2 at the Stanford Synchrotron Radiation Laboratory, Menlo Park, CA. The samples were exposed to polarized monochromatic X-rays of wavelength λ = 1.38 Å (9 keV) for 600 s. Scattered X-rays were observed on a MarCCD detector at a sample-to-detector distance of ∼500 mm along an evacuated flight path. The observable range was $q \simeq 0.05$ to 0.65 Å^{-1}, where q is the scattering vector magnitude, $q = 4\pi\sin(\theta)/\lambda$ (2θ is the scattering angle). The distance between sample and detector was then set to 2 m with λ = 1.24 Å (10 keV) to observe the range $q \simeq 0.01$ to 0.2 Å^{-1}. Experimental parameters, *e.g.* beam center, sample-to-detector distance, detector tilt plane and rotation, were calibrated with a *FIT2D* (Hammersley *et al.*, 1995) analysis of silver behenate (Huang *et al.*, 1993). The temperature was kept constant at 293 K. A background correction was accomplished by subtracting the integrated images of buffer in the solution cell from that of the sample using a scaling factor to line up the higher q region.

The powder rings arising from the random orientation of vesicles were integrated radially (Hammersley *et al.*, 1996), resulting in the so-called '*I*–*q* plot', a one-dimensional profile of X-ray intensity $I(q)$ *versus* scattering vector q. In these experiments, the measured X-ray intensity is an average over the polydisperse vesicle population according to Debye (Guinier, 1994) such that

$$\langle I(q)\rangle = N\langle F(q)^2\rangle + \langle F(q)\rangle^2 \sum^{N}\langle\cos(\mathbf{q}\cdot\mathbf{r}_{nn'})\rangle, \qquad (1)$$

where $F(q)$ is the bilayer form factor, N is the number of particles (vesicles) and $\mathbf{r}_{nn'}$ is the inter-vesicle vector. The first part in equation (1) results from the average scattering of '*N*' individual vesicles, while the second part results from the interference between vesicles and is dependent upon the distance between them, $r_{nn'}$. In this study, no correlation between vesicles was observed, as demonstrated by performing experiments at different vesicle concentrations (not shown), and thus the second term could be neglected. Additionally, from our simulations (not shown), scattering arising from the second term appears at $q \ll 0.01$ Å^{-1} and would not be visible in the q range utilized in this study (see above). Thus we use the simple relation

$$\langle I(q)\rangle \propto \langle F(q)^2\rangle, \qquad (2)$$

where the factor N has been dropped due to arbitrary instrumental scaling. The form factor, $F(q)$, is the Fourier transform of the electron density $\rho(r)$ of the bilayer. The electron density profile across the depth of a bilayer may be viewed as a summation of a total of n Gaussian peaks (one-dimensional) or shells (three-dimensional), each representing a particular lipid moiety or region (Wiener & White, 1992; Pabst *et al.*, 2000). The model accounts for the amplitude ρ_k, average position δ_k and positional uncertainty σ_k of each region k.

$$\rho(r) = \sum_{k=1}^{n} \rho_k \exp[-(r-\delta_k)^2/(2\sigma_k^2)]. \qquad (3)$$

The parameter δ_k is the distance from the center of the vesicle (r = 0) to the bilayer feature and may be alternatively expressed as $\delta_k = R + \varepsilon_k$, where R is the radius of the vesicle and ε_k is the displacement of the feature from R. Note that ε_k may be positive or negative. Typically, a SAXS experiment measures the scattering contrast $\Delta\rho = \rho(r) - \rho_0$, where ρ_0 is the electron density of the buffer. Our analysis method is only concerned with the relative amplitudes of each bilayer feature, not the absolute amplitudes, and so the magnitude of ρ_0 is arbitrary and set equal to zero.

In the case of the flat bilayer model, we assume that the average vesicle is a perfect powder, *i.e.* a collection of flat lipid bilayers with completely random orientation. For a flat lipid bilayer, the form factor $F_f(q)$ is obtained from the one-dimensional Fourier transform (FT) of equation (3):

$$F_f(q) = q^{-1}\sum_{k=1}^{n} \rho_k\sigma_k \exp(-q^2\sigma_k^2/2)\exp(iq\delta_k). \qquad (4)$$

A factor of q^{-1} must be added to relate the one-dimensional FT in the model correctly to the three-dimensional spherical metric of reciprocal space. Others accomplish the same result by adding a Lorentz correction q^{-2} to equation (2) (Pabst *et al.*, 2000). For a perfectly spherical, radially symmetric vesicle composed of n Gaussian shells, the form factor $F_s(q)$ is obtained from the radially symmetric Fourier transform of equation (3), yielding

$$F_s(q) = 2q^{-1}\sum_{k=1}^{n} \rho_k\sigma_k \exp(-q^2\sigma_k^2/2)[\delta_k \sin(q\delta_k) + \sigma_k^2 q\cos(q\delta_k)]. \qquad (5)$$

An expression for the directly measurable quantity $\langle F(q)^2\rangle$ must be obtained from equations (4) and (5). In the case of a flat bilayer $\langle F_f(q)^2\rangle = F_f(q)F_f(q)^*$ and may be expressed as

$$\langle F_f(q)^2\rangle = q^{-2}\sum_{k,k'}^{n}\rho_k\rho_{k'}\sigma_k\sigma_{k'}\exp[-q^2(\sigma_k^2+\sigma_{k'}^2)/2] \times \cos[q(\varepsilon_k-\varepsilon_{k'})] \quad (6)$$

For the spherical vesicle assumption, the polydispersity must be taken into account. We performed a normalized ensemble average over $F_s(q)^2$ (see Appendix *A*) utilizing a Gaussian weight to describe the distribution of vesicles with radii R, average radius R_0 and standard deviation σ_R, resulting in

$$\langle F_s(q)^2\rangle = q^{-2}\sum_{k,k'}^{n}(R_0+\varepsilon_k)(R_0+\varepsilon_{k'})\rho_k\rho_{k'}\sigma_k\sigma_{k'} \times \exp[-q^2(\sigma_k^2+\sigma_{k'}^2)/2]\cos[q(\varepsilon_k-\varepsilon_{k'})], \quad (7)$$

which is nearly identical to equation (6) except for the additional terms which contain the average radius R_0. Note that equation (7) is an approximation valid only in the region of $q \simeq 0.01$ to 1 Å^{-1}, where intensity arising from intra-bilayer features dominates the scattering curve. If smaller angle data ($q \simeq 0.001$ to 0.01 Å^{-1}) were acquired, model fitting with the full expression in equation (5) would enable, additionally, the accurate determination of σ_R.

2.3. Model fitting

A lipid bilayer can be approximately modeled using just three peaks ($n = 3$) where two outer peaks $\rho_{1,3} > 0$ represent the head-groups and an inner peak $\rho_2 < 0$ represents the methyl dip (Pabst *et al.*, 2000). In equation (6), the order of peaks is irrelevant, but for equation (7) we define $k = 1$ to be the inner leaflet peak and $k = 3$ to be the outer leaflet peak. To simplify our model further, we assumed the center of the bilayer to coincide with the center of the methyl region such that $\delta_2 = R_0$, or equivalently $\varepsilon_2 = 0$. Additionally, we normalized each $\rho(r)$ by ρ_2 such that the center peak $\rho_2 = -1$ during curve fitting. These two assumptions reduced the parameter dependency of the fitting procedure and also provide a means of comparing the different models since all results are normalized to the central region of the bilayer. In the case of a symmetric bilayer, all parameters for $k = 1$ and $k = 3$ are equivalent (*e.g.* $\rho_1 = \rho_3$). The data fitting procedure utilized standard non-linear least-squares fitting (NLSF) schemes within *Origin* (OriginLab, USA). The goodness of fit was characterized by values for reduced χ^2 and R^2.

3. Results and discussion

Unilamellar lipid vesicles composed of SOPS at 30 mg ml^{-1} Tris pH 7.6 were exposed to synchrotron X-rays and the resultant two-dimensional image acquired *via* a CCD (Fig. 1*a*). The concentric rings arise from the average scattering of an ensemble of randomly oriented, unilamellar lipid vesicles. A radial integration of the image in Fig. 1(*a*) and additionally for a background sample cell with buffer only (image not shown) result in the *I*–*q* plots shown in Fig. 1(*b*). Three peaks are clearly visible in the lipid data, and after subtracting the background, the scattering arising solely from unilamellar lipid vesicles is shown in Fig. 2(*a*). Note the dramatic improvement in signal-to-noise ratio, especially at higher q, compared with previous work (Pabst *et al.*, 2003; Hirai *et al.*, 2003; Bouwstra *et al.*, 1993). This improvement is accomplished by utilizing an evacuated scattering path, sensitive CCD detector and sample with maximal solute/solvent scattering contrast as described in §2.

The data in Fig. 2(*a*) were then subjected to NLSF utilizing equations (6) and (7). We tried three different models, abbreviated 'flat sym', 'flat asym' and 'sphere', and their fit parameters (Table 1) were used to display the calculated $I(q)$ curves shown superposed on the observed data (Fig. 2*a*). In the flat symmetric bilayer model 'flat sym' (dashed green line) care had to be taken to include an offset in the fit since in theory, the nodes of the form factor and therefore $I(q)$ for a symmetric bilayer should approach 0. This model inadequately describes the observed data as indicated by the poor χ^2 value (Table 1). The fit is dramatically improved by using independent parameters for each leaflet (model 'flat asym', red dashed line in Fig. 2*a*). We then used the parameters from 'flat asym' as starting parameters for the spherical bilayer model 'sphere' but were unable to perform the fit satisfactorily while letting the average vesicles radius R_0 be a free parameter. Under the reasonable assumption that R_0 is fixed at 400 Å for the extruded vesicle sample (MacDonald *et al.*, 1991), the fit was successful (Table 1 and solid blue line in Fig. 2*a*).

In Fig. 2(*b*), $\rho(r)$ calculated according to equation (3) and Table 1 are displayed on a common scale, normalized by the location and magnitude of the methyl dip. For all models, the observed bilayer thickness is $d_{hh} \simeq 42$ Å, in agreement with previous estimates. The green dashed line corresponding to the symmetric flat bilayer produces the familiar shape of a symmetric lipid bilayer (Pabst *et al.*, 2000). For the flat asymmetric model (red dotted line), a remarkable departure from the planar bilayer is observed. One leaflet is both more disordered (larger σ) and thicker (larger ε) than the other. However, from this model, one cannot determine which is the inner and which is the outer leaflet since equation (6) does not contain the $R_0 + \varepsilon_k$ terms essential for this discrimination. The true sidedness of the bilayer is revealed, however, when the spherical model [equation (7)] is used (solid blue line in Fig. 2*b*). Qualitatively, the calculated $\rho(r)$ is similar to that of the flat asymmetric bilayer, *e.g.* it is apparent that both models reveal a thinner higher peak closer to the center of the vesicle and a thicker lower peak further away from the center of the vesicle. However, only the spherical model can correctly discriminate between the two sides of the bilayer.

Hirai *et al.* (2003) also observed leaflet asymmetry and the average vesicle radius of a unilamellar vesicle using a hard-shell model and traditional Guinier analysis. However, these results came from a different analysis: a transform of the intensity was used to elucidate the vesicle radius and model fitting was utilized for the bilayer profile. Additionally, their H_2O/D_2O inverse-contrast method takes advantage of

Table 1
Parameters from NLSF using equations (6) and (7).

$\rho_2 = -1$ and $\varepsilon_2 = 0$ for all fits. ρ is dimensionless while σ, ε and R_0 are in Å.

Model	ρ_1	σ_1	ε_1	σ_2	ρ_3	σ_3	ε_3	R_0	χ^2	R^2
Flat sym	1.71 ± 0.01	3.43 ± 0.04	−20.9 ± 0.04	7.79 ± 0.07	1.71 ± 0.01	3.43 ± 0.04	20.9 ± 0.04	–	0.289	0.996
Flat asym	1.18 ± 0.03	4.87 ± 0.13	−22.4 ± 0.42	7.67 ± 0.07	2.78 ± 0.04	2.11 ± 0.06	19.6 ± 0.46	–	0.036	0.999
Sphere	1.25 ± 0.04	4.79 ± 0.17	−22.2 ± 0.56	7.75 ± 0.19	2.50 ± 0.04	2.32 ± 0.07	19.8 ± 0.69	400†	0.037	0.999
Sphere*	1.31 ± 0.01	5.34 ± 0.05	−23.2 ± 0.12	8.10 ± 0.12	2.54 ± 0.02	2.25 ± 0.03	18.4 ± 0.09	376 ± 2	< 0.001	0.999

† Held constant during fitting.

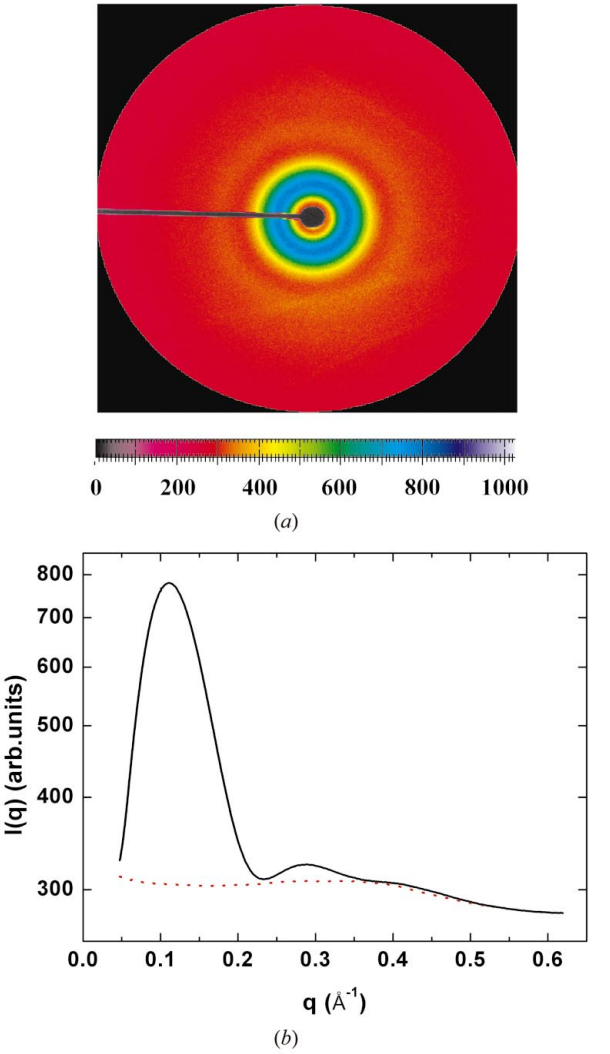

Figure 1
(*a*) 2k × 2k MarCCD image displayed by *FIT2D* (Hammersley *et al.*, 1996) of X-ray scattering from SOPS unilamellar vesicles. The thin black line is from the beamstop fixture and is excluded from radial integration. (*b*) Radial integration of image (*a*) (black solid line) and radial integration of a background image (red dashed line).

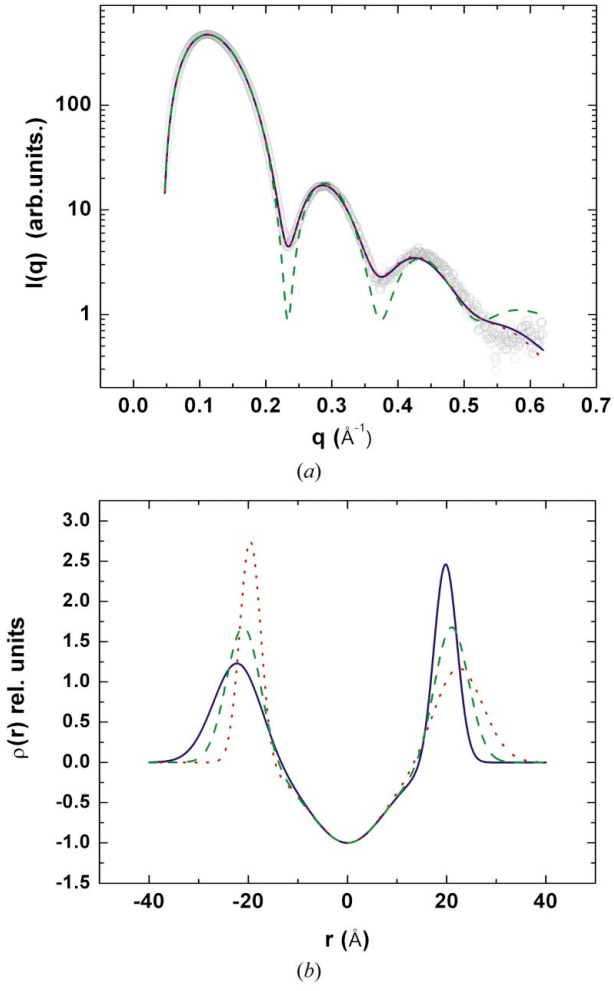

Figure 2
(*a*) Background-corrected $I(q)$ profiles from unilamellar SOPS vesicles. NSLF-fitted scattering curves according to 'sphere' (solid blue line), 'flat asym' (red dotted line) and 'flat sym' (dashed green line) models are superposed on the data. (*b*) Calculated $\rho(r)$ according to 'sphere' (solid blue line), 'flat asym' (red dotted line) and 'flat sym' (dashed green line) models.

differing scattering length densities for the specific molecular species present in their sample. This information is extremely valuable in providing physiochemical constraints in model fitting. Although their hard-shell model revealed five 'features' in the electron density profile, it must be noted that the resolution is limited by the use of this shell model. By definition, electron density is the probability of finding an electron (or in this case lipid moiety) in the given region. In the case of the hard-shell model, all points within the shell are equally probable, *i.e.* a bilayer of thickness 32.9 Å is just as likely as one of 50.5 Å (and all values between). Our approach improves on the Guinier hard-shell method by (i) providing a single analytic expression describing vesicle radius as well as the electron density profile, and (ii) utilizing Gaussian functions which define a most probable location and standard

deviation of each bilayer feature. This results in higher accuracy for $\rho(r)$ and a more physical depiction of a lipid vesicle.

From simulations of X-ray scattering profiles according to equation (1) using all terms (see Appendix *A*), we found that, as expected, the scattering curve region $q \simeq 0.05$ to 0.65 Å^{-1} is most sensitive to bilayer profile parameters, while R_0 and σ_R (as well as inter-vesicle interactions) have the greatest effect in the small-angle region of $q \simeq 0.001$ to 0.05 Å^{-1} (not shown). This is, of course, due to the relation $q = 2\pi/d$, where d is the real-space quantity associated with q.

To ascertain a fitted value for R_0, we performed an additional SAXS experiment under the conditions given in §2 on the same sample and acquired an image corresponding to the range $q \simeq 0.01$ to 0.2 Å^{-1}, although the most sensitive region of $q \simeq 0.001$ to 0.01 Å^{-1} could not be reached under the experimental conditions. Shown in Fig. 3(*a*) is the baseline-corrected *I*–*q* plot (blue squares) displayed simultaneously with the data from Fig. 2(*a*) (gray circles). Both data sets were normalized at the $q \simeq 0.14$ Å^{-1} peak. We then performed NLSF on both data sets simultaneously using the 'sphere' model, starting from the parameters of model 'sphere' in Table 1 and allowing the vesicle radius to vary. The results ('sphere*' in Table 1) are similar to those for 'sphere' yet additionally uniquely determine the average vesicle radius of 376 ± 2 Å. The calculated $I(q)$ profile with parameters from sphere* (red line) is superposed on the extended data set in Fig. 3(*a*).

A plausible model of the SOPS vesicle bilayer is presented in Fig. 3(*b*), which shows a cross section of the vesicle bilayer of average radius 376 Å and $\rho(r)$ according to the fit parameters from model 'sphere*' in Table 1. Note how the inner leaflet is depicted as rougher, *i.e.* a larger variation in head-group positions. This provides a plausible explanation for the larger σ and ε observed for the inner leaflet as opposed to the smoother outer leaflet whose head-groups are distributed in a much narrower region. This packing arrangement could provide relief from the postulated negative curvature strain of the inner leaflet.

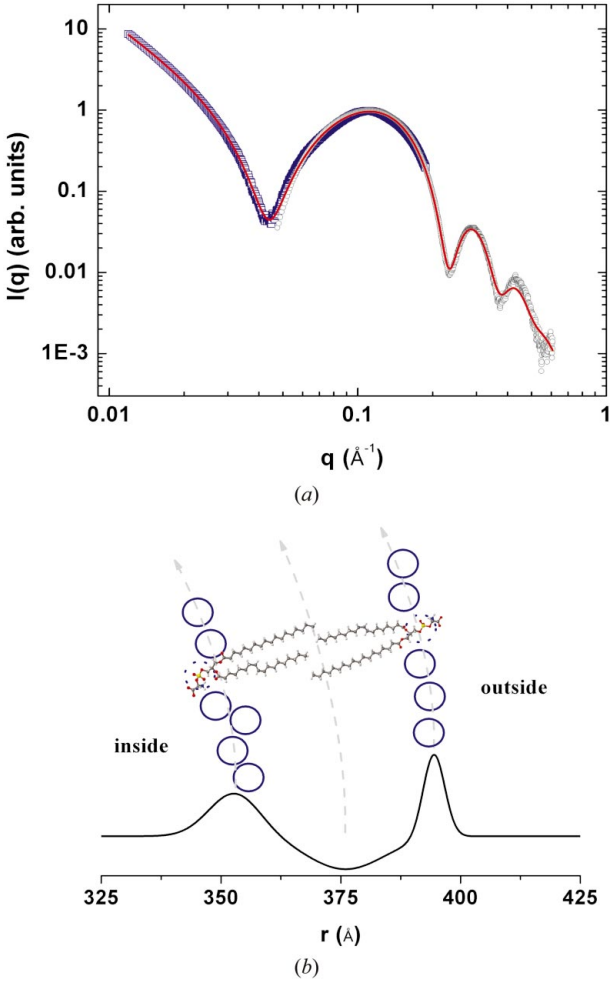

Figure 3
(*a*) Composite data set including data from Fig. 2(*a*) (gray circles) and smaller angle data (blue squares), with superposed calculated $I(q)$ profile (red line) according to the fit parameters of model 'sphere*'. (*b*) Hypothetical model of the vesicle bilayer. Shown is the calculated $\rho(r)$ profile obtained with parameters from 'sphere*', along with a depiction of the bilayer structure and arrangement. Blue circles represent plausible head-group locations. Models of SOPS are shown for reference.

4. Conclusions

In summary, a relatively simple yet robust analytical expression completely describing the structure of a unilamellar lipid vesicle was derived from fundamental X-ray scattering theory. Straightforward SAXS experiments enabled us to test these expressions with remarkable results: (i) both flat and spherical models are capable of elucidating the general shape of a lipid bilayer, and (ii) a spherical treatment simultaneously reveals the average radius and asymmetry of the vesicle. We find that SOPS unilamellar vesicles are 'rougher' on their inner leaflet.

Considering the improvement in data fitting when adding smaller angle data, we plan to pursue an even smaller angle regime. SANS (Nieh *et al.*, 2004; Hirai *et al.*, 2003) and SAXS (Lesieur *et al.*, 2000) curves clearly show distinct 'wiggles' at $q \simeq 0.01$ Å^{-1}, which in our simulations are the result of small changes to R_0 and σ_R. We anticipate that our ultra-small-angle X-ray scattering (USAXS) experiments, currently in progress, will extend the result of the current work, enabling us to measure simultaneously the complete electron density profile, average radius, polydispersity and inter-vesicle distances of a vesicle population.

APPENDIX *A*
Derivation of equation (7)

Here we present the derivation for the expression in equation (7). Starting with the form factor for a spherical vesicle [equation (5)],

$$F_s(q) = q^{-1} \sum_{k=1}^{n} 2\rho_k\sigma_k \exp(-q^2\sigma_k^2/2)\big[\delta_k \sin(q\delta_k) + \sigma_k^2 q \cos(q\delta_k)\big], \quad (8)$$

we simplify further calculations by dropping the insignificant second term such that

$$F_s(q) = 2q^{-1} \sum_{k=1}^{n} \delta_k \rho_k \sigma_k \exp(-q^2\sigma_k^2/2) \sin(q\delta_k). \quad (9)$$

The square of equation (9) is a series of all possible combinations over k and k':

$$F_s(q)^2 = 4q^{-2} \sum_{k,k'}^{n} \delta_k \delta_{k'} \rho_k \rho_{k'} \sigma_k \sigma_{k'} \exp[-q^2(\sigma_k^2 + \sigma_{k'}^2)/2] \times \sin(q\delta_k) \sin(q\delta_{k'}). \quad (10)$$

Using a Gaussian distribution to describe vesicle size (see text) and including the relation $\delta = R + \varepsilon$, the normalized ensemble average is

$$\langle F_s(q)^2 \rangle = \frac{\int_{R_0-\alpha}^{R_0+\alpha} \exp[-(R-R_0)^2/(2\sigma_R^2)] F_s(q)^2 \, dR}{\int_{R_0-\alpha}^{R_0+\alpha} \exp[-(R-R_0)^2/(2\sigma_R^2)] \, dR}, \quad (11)$$

where the limit α is equivalent to infinity since the functions are well behaved. Others have used $\alpha = 3\sigma_R$ (Kiselev *et al.*, 2001).

Performing the integral in equation (11) yields the full expression for the average of the squared form factor given as

$$\langle F_s(q)^2 \rangle = 2q^{-2} \sum_{k,k'}^{n} \rho_k \rho_{k'} \sigma_k \sigma_{k'} \exp[-q^2(\sigma_k^2 + \sigma_{k'}^2)/2] \times [A(q) - B(q) + C(q)] \quad (12)$$

with the relations

$$A(q) = [(R_0 + \varepsilon_k)(R_0 + \varepsilon_{k'}) + \sigma_R^2] \cos[q(\varepsilon_k - \varepsilon_{k'})], \quad (13)$$

$$B(q) = \exp(-2q^2\sigma_R^2)[(R_0 + \varepsilon_k)(R_0 + \varepsilon_{k'}) + \sigma_R^2 - 4q^2\sigma_R^4] \times \cos[q(2R_0 + \varepsilon_k + \varepsilon_{k'})] \quad (14)$$

and

$$C(q) = 2\sigma_R^2 q \exp(-2q^2\sigma_R^2)(2R_0 + \varepsilon_k + \varepsilon_{k'}) \times \sin[q(2R_0 + \varepsilon_k + \varepsilon_{k'})]. \quad (15)$$

Note that if $\sigma_R = 0$, equation (12) returns to equation (10). In the q region observed in this work, only the first term $A(q)$ is significant. Additionally σ_R^2 and the factor of 2 are dropped since they are lost in relating $I(q)$ to $\langle F(q)^2 \rangle$ [equation (2)] where $I(q)$ has arbitrary units. The final expression used in the model fitting [equation (7)] is then

$$\langle F_s(q)^2 \rangle = q^{-2} \sum_{k,k'}^{n} (R_0 + \varepsilon_k)(R_0 + \varepsilon_{k'}) \rho_k \rho_{k'} \sigma_k \sigma_{k'} \times \exp[-q^2(\sigma_k^2 + \sigma_{k'}^2)/2] \cos[q(\varepsilon_k - \varepsilon_{k'})]. \quad (16)$$

We acknowledge Vadim Cherezov, Lin Yang, Hiro Tsuruta and members of the Brunger laboratory for their stimulating discussions and critical reading of the manuscript. This work was supported in part by NIH grant 1-RO1-MH63105-01 to ATB. Portions of this research were carried out at the Stanford Synchrotron Radiation Laboratory, a national user facility operated by Stanford University on behalf of the US Department of Energy, Office of Basic Energy Sciences. The SSRL Structural Molecular Biology Program is supported by the Department of Energy, Office of Biological and Environmental Research, and by the National Institutes of Health, National Center for Research Resources, Biomedical Technology Program.

References

Bouwstra, J. A., Gooris, G. S., Bras, W. & Talsma, H. (1993). *Chem. Phys. Lipids*, **64**, 83–98.
Gennis, R. B. (1989). Editor. *Biomembranes: Molecular Structure and Function*. New York: Springer-Verlag.
Guinier, A. (1994). Editor. *X-ray Diffraction in Crystals, Imperfect Crystals and Amorphous Bodies*. New York: Dover.
Hammersley, A. P., Svensson, S. O., Hanfland, M., Fitch, A. N. & Hdusermann, D. (1996). *High Pressure Res.* **14**, 235–248.
Hammersley, A. P., Svensson, S. O., Thompson, A., Graafsma, H., Kvick, E. & Moy, J. P. (1995). *Rev. Sci. Instrum.* **66**, 2729–2733.
Hirai, M., Iwase, H., Hayakawa, T., Koizumi, M. & Takahashi, H. (2003). *Biophys. J.* **85**, 1600–1610.
Huang, T. C., Toraya, H., Blanton, T. N. & Wu, Y. (1993). *J. Appl. Cryst.* **26**, 180–184.
Katsaras, J. & Gutberlet, T. (2001). *Lipid Bilayers, Structure and Interactions*. New York: Springer-Verlag.
Kiselev, M. A., Lesieur, P., Kisselev, A. M., Lombardo, D., Killany, M. & Lesiur, S. (2001). *J. Alloys Compd.* **328**, 71–76.
Lesieur, P., Kiselev, M. A., Barsukov, L. I. & Lombardo, D. (2000). *J. Appl. Cryst.* **33**, 623–627.
MacDonald, R. C., MacDonald, R. I., Menco, B. Ph. M., Takeshita, K., Subbarao, N. K. & Hu, L.-R. (1991). *BBA*, **1061**, 297–303.
Nieh, M. -P., Harroun, T. A., Raghunathan, V. A., Glinka, C. J. & Katsaras, J. (2004). *Biophys. J.* **86**, 2615–2629.
Pabst, G., Koschuch, R., Pozo-Navas, B., Rappolt, M., Lohner, K. & Laggner, P. (2003). *J. Appl. Cryst.* **36**, 1378–1388.
Pabst, G., Rappolt, M., Amenitsch, H. & Laggner, P. (2000). *Phys. Rev. E*, **62**, 4000–4009.
White, S. H. & Hristova, K. (2001). In *Lipid Bilayers, Structure and Interactions*, edited by J. Katsaras & T. Gutberlet. New York: Spinger-Verlag.
Wiener, M. C. & White, S. H. (1992). *Biophys. J.* **61**, 434–447.